

Supporting Information

for

**Air exposed 1,4-bis(trimethylsilyl)-1,4-dihydropyrazine: an
avant-garde carbonization precursor for multi-
functionalized carbon material**

Shaikh Saddam Shoukat Ali^a, Kingshuk Roy^{a,c}, Naveenkumar Akula^a, Satishchandra B. Ogale^{b,c} and Moumita Majumdar^{*a}

Contents

1.	Experimental Detail	2
2.	NMR spectra	4
3.	APC	6
4.	Optical Spectroscopy	6
5.	XPS	7
6.	Elemental Composition	9
7.	Probable Structures	10
8.	DFT Calculations	11
9.	X-ray Data	12
10.	TGA	13
11.	FE-SEM	14
12.	TEM	15
13.	Electrochemical Performance	16

[a] Department of Chemistry,
Indian Institute of Science, Education and Research, Pune
Pune-411008, Maharashtra
India
E-mail: moumitam@iiserpune.ac.in

[b] Department of Physics,
Indian Institute of Science, Education and Research, Pune
Pune-411008, Maharashtra
India

[c] Research Institute for Sustainable Energy (RISE), TCG Centres for Research and Education in Science and Technology (TCG-CREST), Omega, BIPL Building, Blocks EP & GP, Sector V, Salt Lake, Kolkata 700091, India.

1. Experimental Detail

General Remarks.

Syntheses: All chemicals were purchased from Sigma-Aldrich and used as it is. Tetrahydrofuran and pentane were refluxed over sodium/benzophenone and distilled prior to use. Dimethyl formamide was used for emission spectroscopy. 1,4-Bis-(trimethylsilyl)-1,4-diaza-2,5-cyclohexadiene **1** was prepared according to literature procedure.^[S1] Tetrahydrofuran-*d*₈ and dimethyl sulfoxide-*d*₆ were used as purchased. Annealing was done in Nabertherm RHTC 80-710/15. Distilled acetonitrile solvent was used for drop casting **3** on grids for FE-SEM and TEM measurements.

Characterization: ¹H, and ¹³C{¹H} NMR spectra were referenced to external SiMe₄ using the residual signals of the deuterated solvent (¹H) or the solvent itself (¹³C). ²⁹Si{¹H} NMR spectra were referenced to external SiMe₄. Molecular weights and molecular weight distributions (dispersity (*D*)) of polymers were determined by Waters ACQUITY Advanced Polymer Chromatography (APC). The instrument contains a 1500 series HPLC pump, an ACQUITY® refractive index (RI) detector, one ACQUITY APC™ XT 2002.5 μm (4.6 × 7.5 mm) column in DMF at 45 °C at 0.25 mL/min flow rate. Polystyrene (PS) standards were used to calibrate the instrument. UV/vis spectrum was acquired using a Shimadzu UV-3600 Plus UV-Vis/NIR spectrophotometer. The emission spectrum was recorded using Synergy Micro plate Reader (BIOTEK USA) by exciting at 255, 379 and 491 nm. Excitation and emission band width of equipment were kept at 16.0 nm. Fourier transform infrared (FTIR) spectroscopic measurements for **2** and **3** were done on KBr pellets using Thermo scientific NICOLET 6700 FTIR spectrophotometer. X-ray photoelectron spectroscopy (XPS) data were collected by using AXIS Supra, Kratos Analytical, UK. Scanning Electron Microscopy (SEM) was done using FEI Nova Nano 450 SEM. CHN analyses were performed on Elementar vario EL analyzer. Thermogravimetric analysis of **1** and **2** were performed under a flow of N₂ (heating rate: 10 degree/min) using Setsoft 2000 (Setaram Instrumentation). Powder X-ray Diffraction (XRD) of **3** was recorded using a Bruker D8 Advance X-ray diffractometer equipped with Cu Kα radiation (1.54 Å). Raman spectrum of **3** was analysed by using LabRAM HR800 from Yvon Horiba (λ_{max} = 633 nm laser). Transmission Electron Microscopy (TEM) images were taken using JEM 2200FS TEM microscope operating at an accelerating voltage of 200 kV. Thermogravimetric analysis of **3** was performed in air (heating rate: 10 degree/min) using TGA Perkin-Elmer STA6000. Thermogravimetric (TG), differential thermal analysis and mass spectra of the evolved gas during the thermal decomposition of **2** were studied on TA Instruments SDT Q600 coupled to Discovery MS, using open alumina crucible, containing sample weighing about 50 mg with a linear heating rate of 4 degrees/min up to 700 °C and then isothermally for 20 mins under a flow of Argon.

Electrode and coin half-cell fabrication: The electrodes of the material are prepared by mixing the active material **3**, multi-walled carbon nanotubes (MWCNT) and PVDF (Polyvinylidene difluoride, Sigma Aldrich) binder (Weight ratios were maintained as 8:1:1) in *N*-Methyl-2-pyrrolidone (NMP) solvent followed by coating the slurry onto a Cu foil. Then the electrodes are dried in the oven at 80°C overnight.

The foil was then punched into 1 cm² circular discs. The CR-2032 coin half-cell was assembled using this composite as the working electrode and metallic lithium foil as the counter and reference electrode. The mass of active material loaded on the electrode was 1.1 mg. 1M lithium hexafluorophosphate (LiPF₆) electrolyte was used in a solvent combination of 1:1 Ethylene carbonate (EC) and Dimethyl carbonate (DMC) along with 5 wt.% Fluoroethylene Carbonate (FEC, Sigma Aldrich) as additive. Celgard 2500 was used as the separator. All the cells were assembled inside an Argon-filled glove box.

Total amount of electrolyte used was 150 μl for each cell.

Measurements: Cyclic voltammetry was performed in Ametek potentiostat at a scan-rate of 0.2 mV/s keeping the vertex potentials from 0.01 to 3 V. The galvanostatic charge-discharge measurements are carried out in NEWARE corporation battery analyser at a current density of 100 mA g⁻¹. Rate capability was evaluated under a wide range of

current densities from 0.1 A/g to 4 A/g. The potentiostatic electrochemical impedance spectroscopy was performed in the Ametek potentiostat instrument in a frequency ranging from 300 KHz to 100 mHz.

Synthesis of 2: 5 g of 1,4-bis-(trimethylsilyl)-1,4-dihydropyrazine **1** was dissolved in 15 mL of pentane maintaining inert atmosphere conditions. The bright yellow solution was then poured into a petri-dish and exposed to air. The solvent evaporated and an orange solid **2** was obtained within a span of 4 hours of air exposure.

¹H NMR (400 MHz, DMSO-*d*₆): δ 9.8 (broad, -NH or -OH); 8.8-7.6 (aromatic -CH); 6.2-4.5 (alkenyl protons); 3.36 (water in dmsO-*d*₆); 2.50 (residual proton in dmsO-*d*₆); 1.2-0.8 (pentane protons); 0.08 to -0.1 (siloxane protons) ppm.

¹³C{¹H} NMR (101 MHz, DMSO-*d*₆): δ 165-158 (aromatic C); 140-100 (C=C); 79-72 (C=C in the chromophores); 35-30 (solvent); 2.5-2.0 (siloxane C) ppm.

²⁹Si{¹H} (79.53 MHz, THF-*d*₈): +7.09 ((Me₃Si)₂O) ppm (detected during *in situ* conversion of **1** to **2** in THF-*d*₈ medium taken in an open NMR tube).

FT-IR (in cm⁻¹): 3600-3000 (strong and broad, O-H and N-H stretching); 3000 (medium, C-H stretching); 1680 (strong, amide C=O stretching); 1597 (C=N stretching); 1523 (N-O stretching); 1396 (phenolic O-H bending); 1250 (C-N stretching); 1070 (C-O stretching); 883 (out-of-plane C-H); 753 (N-H wagging); 657 (=C-H bending).

Synthesis of 3: 1 g of **2** was annealed up to 700 °C under argon containing 10% of dihydrogen in a furnace and then holding the temperature for 20 minutes to yield a black powder **3**. The rate of heating was 4 degree/min.

FT-IR (in cm⁻¹): 3423 (strong, O-H stretching); 3159 (strong, N-H stretching); 3000 (medium, C-H stretching); 1619 (strong, C=C stretching); 1523 (N-O stretching); 1396 (phenolic O-H bending); 1270 (C-N stretching); 1090 (C-O stretching); 1038 (C-O-C stretching); 869 (out-of-plane C-H); 805 (C=C bending); 615 (=C-H bending).

2. NMR Spectra

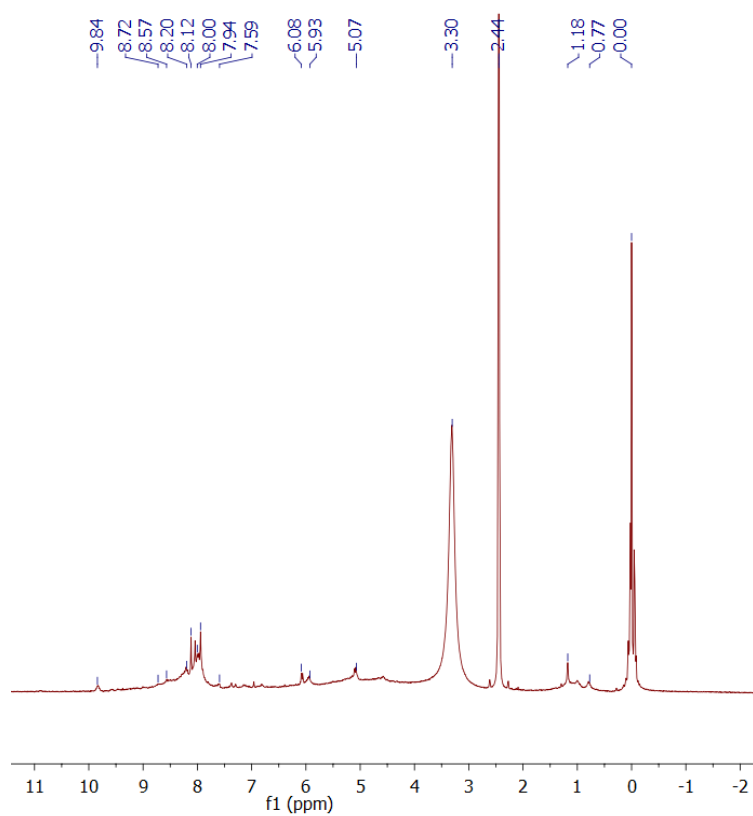


Figure S1. ¹H NMR spectrum of **2** in dms0-*d*₆

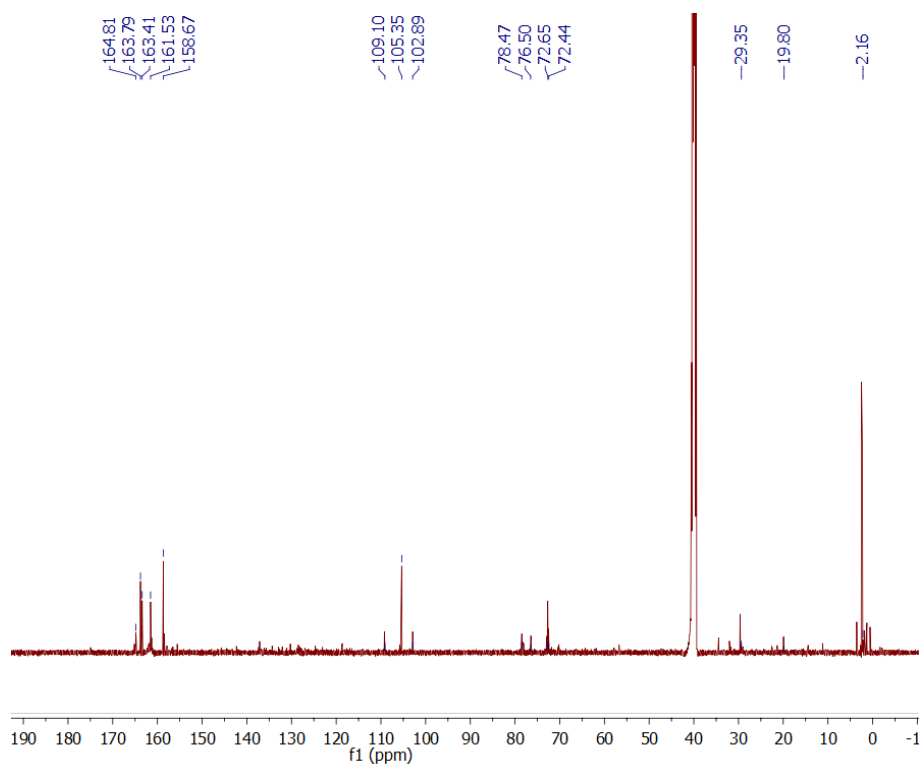


Figure S2. ¹³C NMR spectrum of **2** in dms0-*d*₆

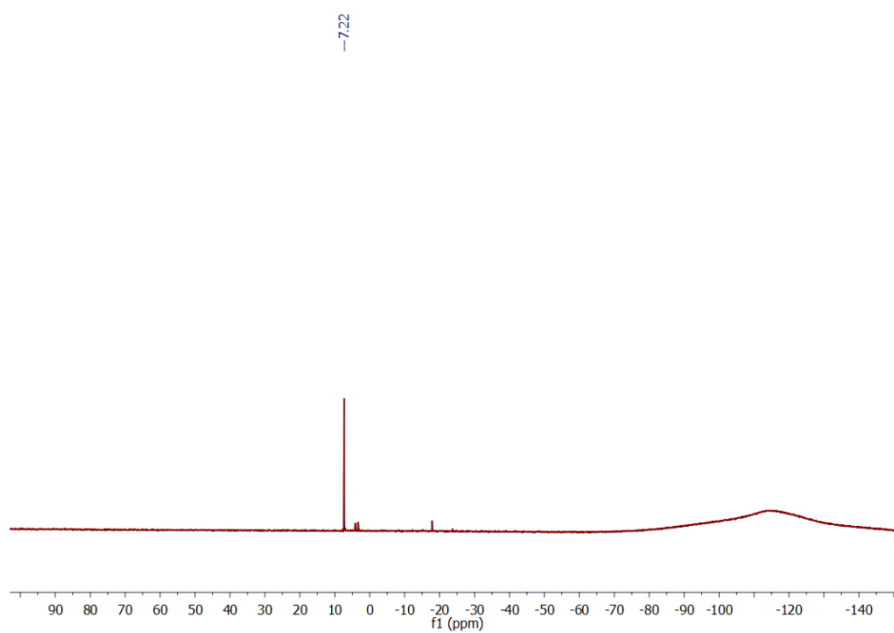


Figure S3. ^{29}Si NMR spectrum of **2** in $\text{dms0-}d_6$

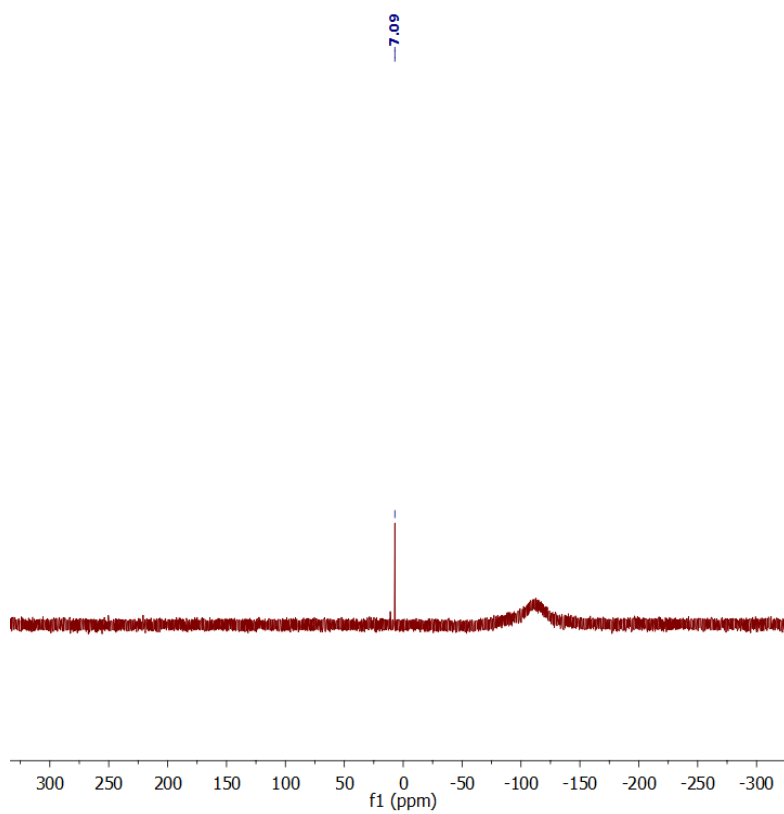


Figure S4. ^{29}Si NMR spectrum of *in-situ* generated **2** in $\text{THF-}d_8$

3. Advanced Polymer Chromatography

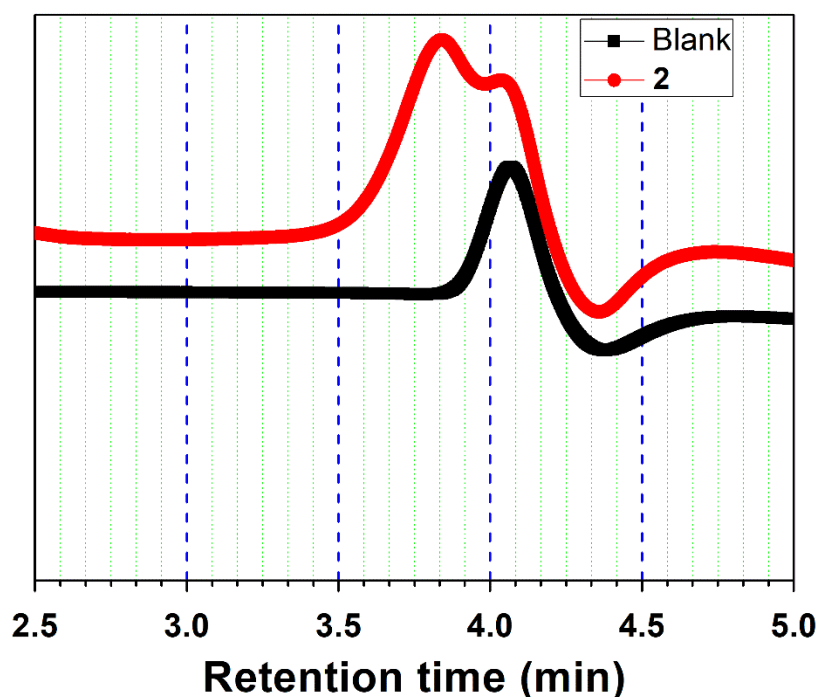


Figure S5. Advanced Polymer Chromatography (APC) of **2** showing a high molecular weight polymeric species with a weight average molecular mass (M_w) of 5.4 kDa and number average molecular mass (M_n) of 4.6 kDa, giving a polydispersity index (M_w/M_n) of 1.18.

4. Optical Spectroscopy

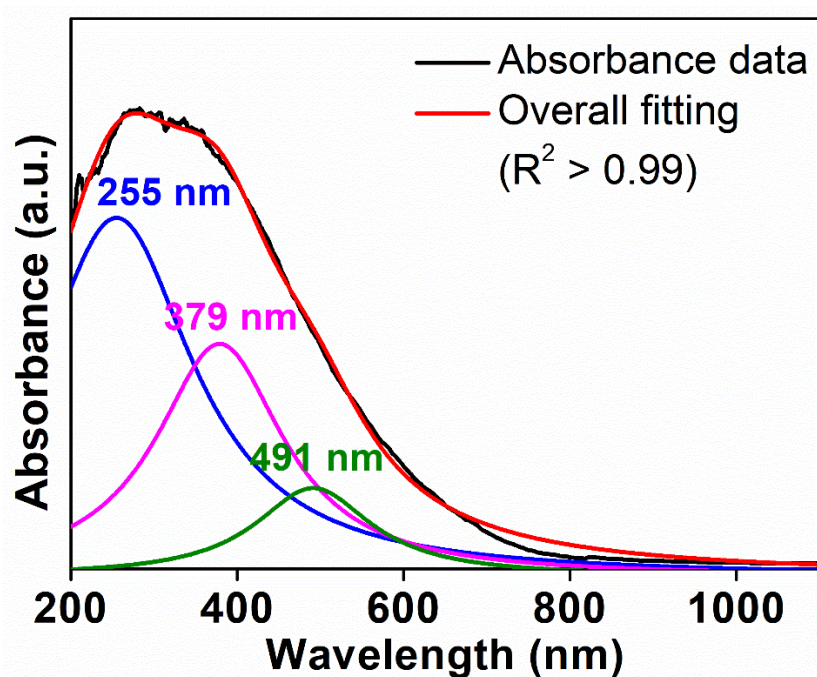


Figure S6. Absorbance spectrum of **2**

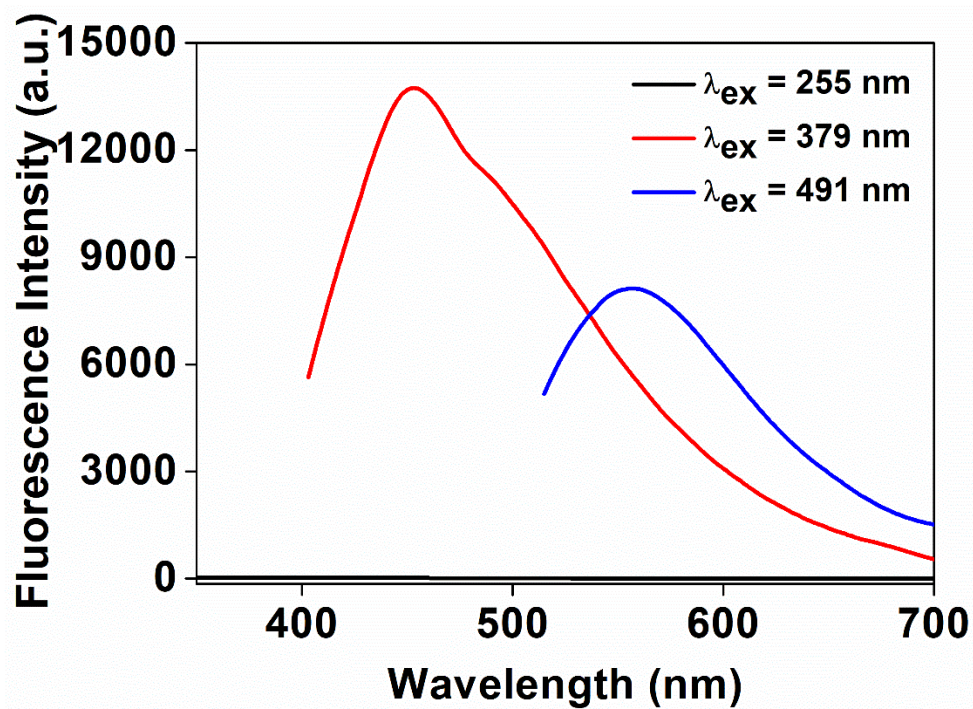


Figure S7. Emission spectrum of 2

5. XPS Spectra

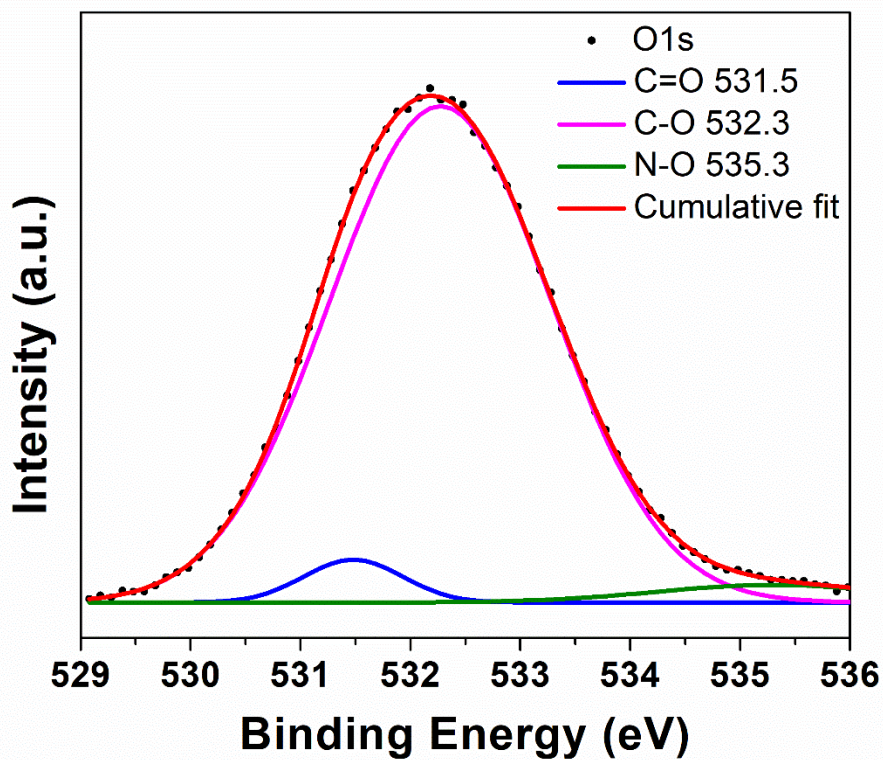


Figure S8. High resolution O1s XPS spectrum of 2

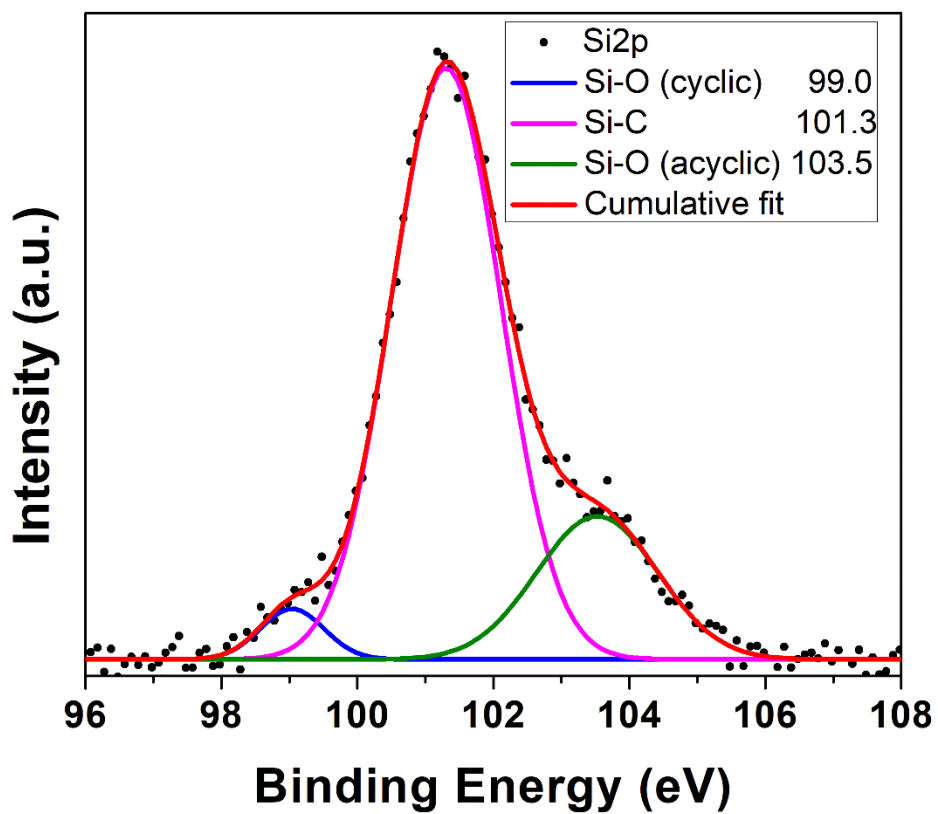


Figure S9. High resolution Si2p XPS spectrum of 2

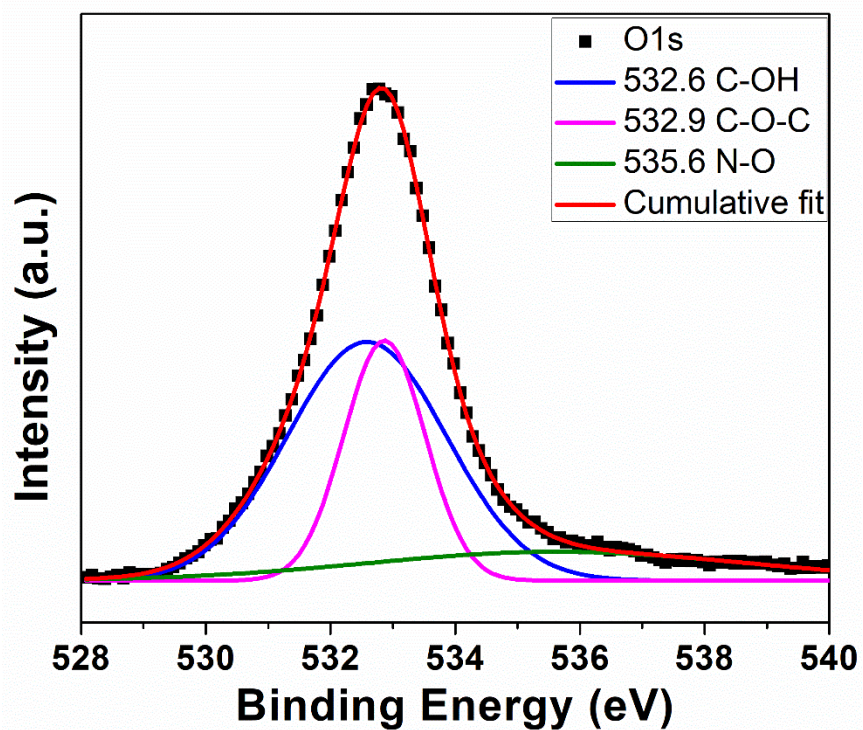


Figure S10. High resolution O1s XPS spectrum of 3

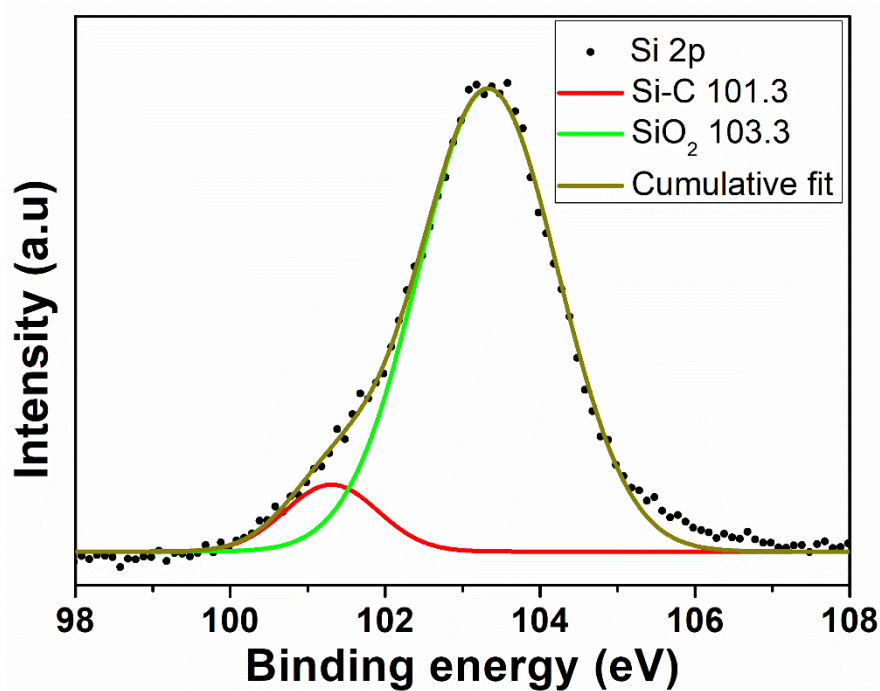


Figure S11. High resolution Si2p XPS spectrum of **3**

6. Elemental Composition

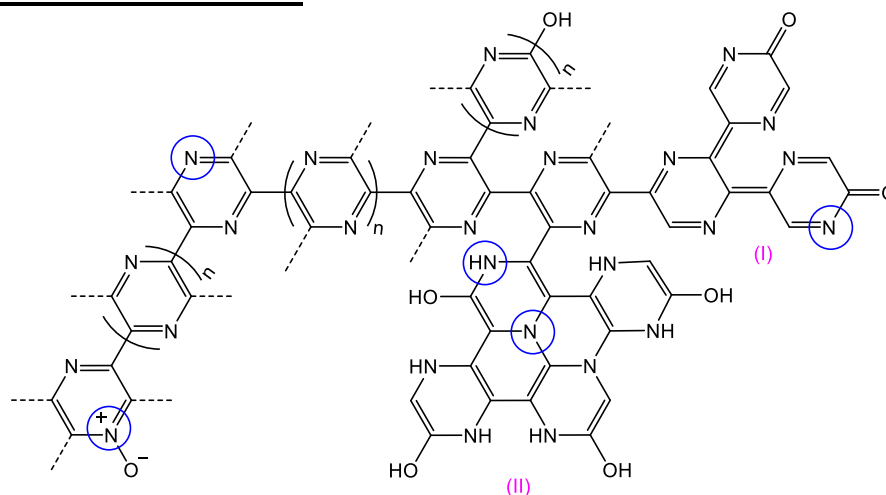
Table S1. Elemental Composition Data in wt% for **2** and **3**

	XPS		CHN		FE-SEM		Overall Composition ^a	
	2	3	2	3	2	3	2	3
C	52.50	73.84	50.65	71.29	52.67	73.15	50.65	71.29
N	22.63	10.07	22.51	10.01	24.09	10.60	22.51	10.01
O	19.64	12.26	-	-	17.29	12.35	17.77	11.94
H	-	-	3.68	3.01	-	-	3.68	3.01
Si	5.23	3.83	-	-	5.95	3.90	5.39	3.75

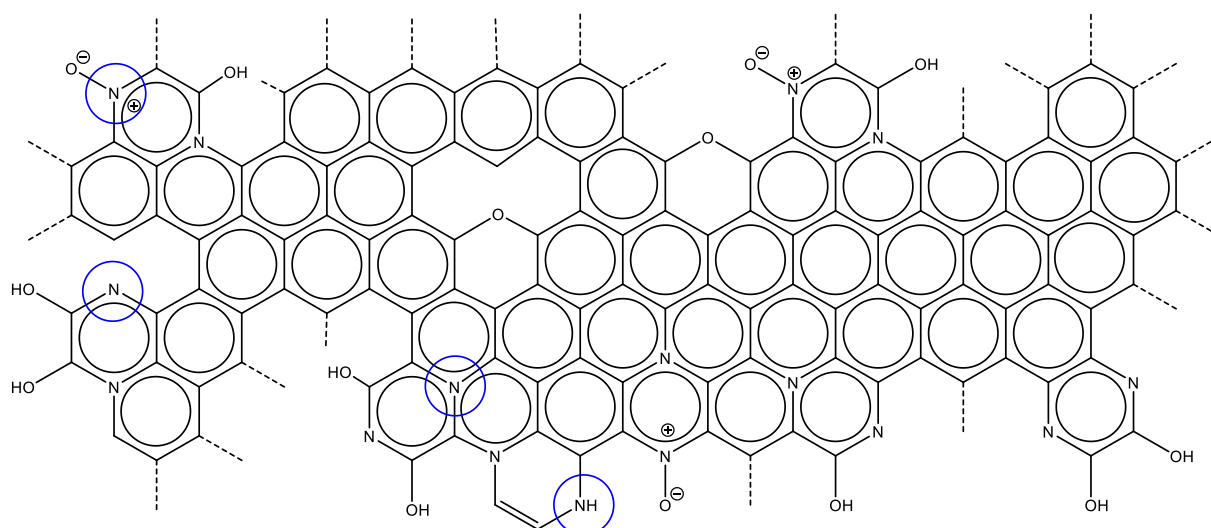
^a

The overall composition has been derived considering the absolute values of C, H and N wt% obtained from CHN analysis, C/O and C/Si ratios from XPS and FE-SEM analyses.

7. Probable structures of 2 and 3



Scheme S1. Probable structure of **2**. The different types of Ns have been marked in blue. Two proposed chromophores (I and II) have mentioned. The dotted lines represent the probable branching of polymer. *Note:* small amounts of cyclic and acyclic siloxanes are present along with **2**.



Scheme S2. Probable structure of **3**. The different types of Ns have been marked in blue. The dotted lines represent the probable extension of the carbon material. *Note:* The 1,4-positions of the Ns in the rings might not be strictly maintained ^[S2] and the positions of the graphitic Ns can also be elsewhere within the framework. Small amounts of SiO₂ are present along with **3**.

8. DFT Calculations

DFT calculations were performed on the proposed chromophores I and II in **2**, at the B3LYP level of theory (6-31G(d,p) basis set for C, N, O and H using *Gaussian 09* suite of programs.^[S3] Both chromophores were optimized at the stationary point with number of imaginary frequency NIMAG = 0. TD-DFT were performed on the optimized geometries of I and II at the same level of theory and using same basis sets.

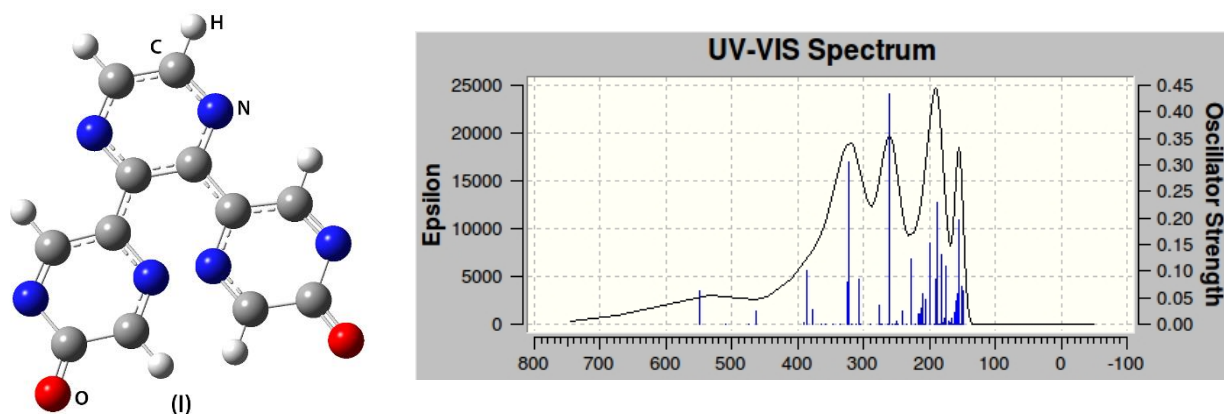


Figure S12. Optimized geometry of the proposed chromophore I in **2** and the absorbance spectrum.

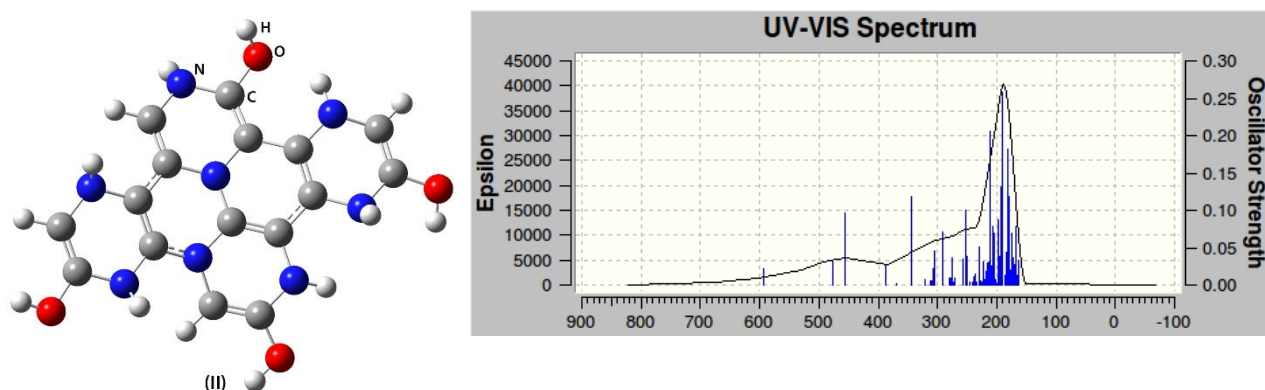


Figure S13. Optimized geometry of the proposed chromophore II in **2** and the absorbance spectrum.

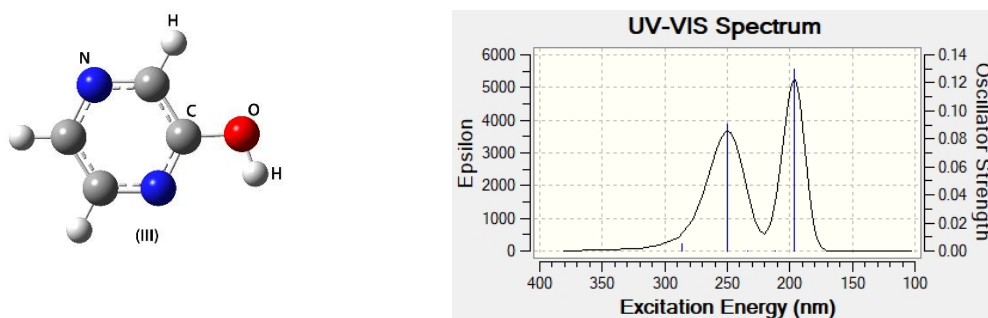


Figure S14. Optimized geometry of the proposed chromophore III in **2** and the absorbance spectrum.

9. X-ray Data of 2,3,5,6-tetramethyl pyrazine

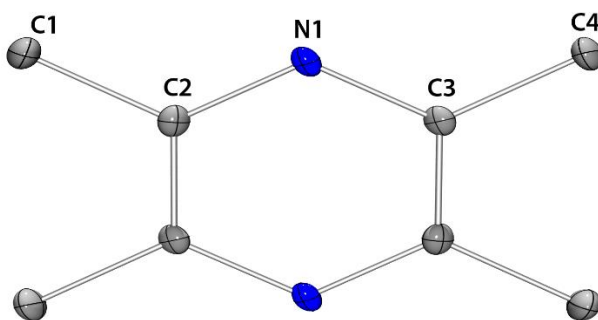


Figure S15. Molecular structure of 2,3,5,6-tetramethyl pyrazine obtained when 2,3,5,6-tetramethyl-1,4-bis(trimethylsilyl)-1,4-dihydropyrazine was exposed to air. Ellipsoid probability of 30% and H atoms, H₂O molecules were removed for clarity.

Table S2. Crystal data and structure refinement for 2,3,5,6-tetramethyl pyrazine ^[S4]

Empirical formula	C ₈ H ₁₂ N ₂ ·(H ₂ O) ₃
Formula weight	190.24
Temperature	100(2) K
Wavelength	1.54178 Å
Crystal system	monoclinic
Space group	P 2 ₁ /c
Unit cell dimensions	a = 6.9291(14) Å α = 90 ° b = 13.388(3) Å β = 101.950(14) ° c = 11.671(2) Å γ = 90 °
Volume	1059.2(4) Å ³
Z	4
Density (calculated)	1.193 Mg/m ³
Absorption coefficient	0.751 mm ⁻¹
F (000)	416
Crystal size	0.1 x 0.08 x 0.07 mm ³
Theta range for data collection	5.091 to 66.757 °
Index ranges	-8 ≤ h ≤ 8, -15 ≤ k ≤ 15, -13 ≤ l ≤ 13
Reflections collected	1559
Independent reflections	7449
Completeness to theta = 66.757°	97.1 %
Absorption correction	none
Max. and min. transmission	0.985 and 0.965
Refinement method	Full-matrix least-squares on F ²
Data / restraints / parameters	1816 / 6 / 146
Goodness-of-fit on F ²	1.029
Final R indices [I > 2σ(I)]	R1 = 0.0628, wR2 = 0.1346
R indices (all data)	R1 = 0.1146, wR2 = 0.1537
Largest diff. peak and hole	0.302 and -0.267 eÅ ⁻³

10. Thermogravimetric Analysis

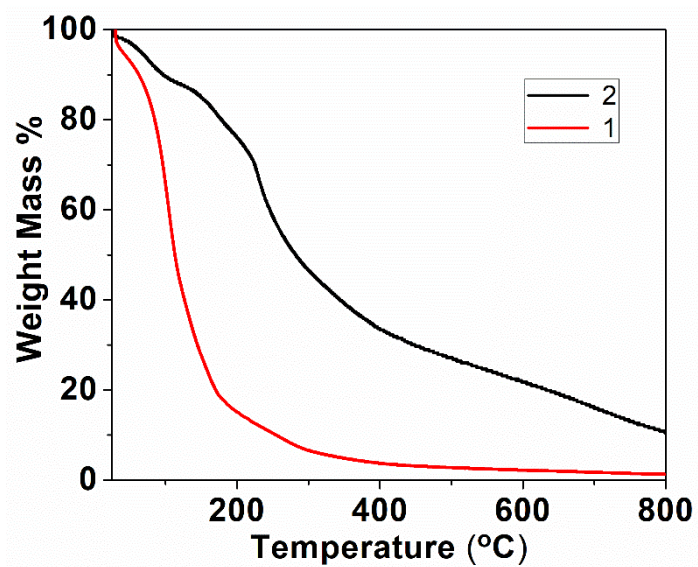


Figure S16. TGA of 1 and 2 in N₂.

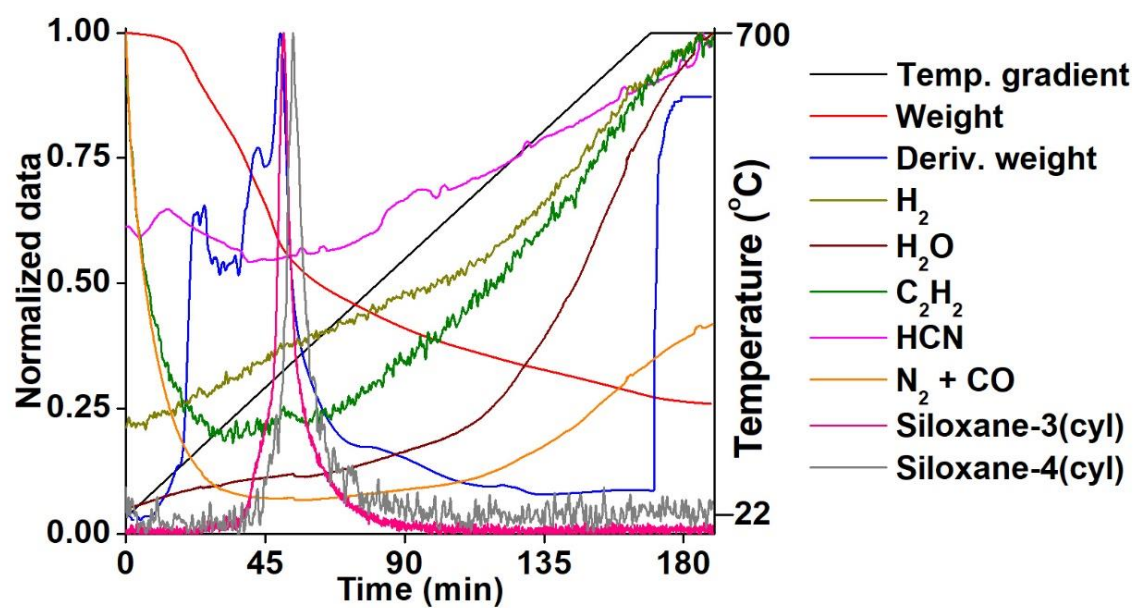


Figure S17. TG-MS of 2 in Argon.

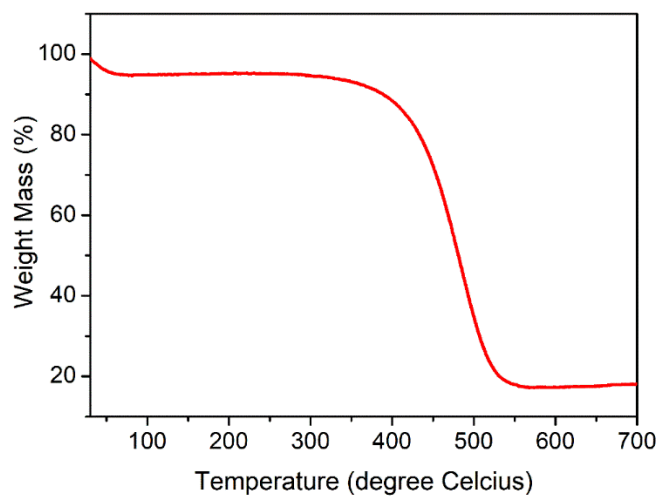


Figure S18. TGA of 3 in air

11. FE-SEM

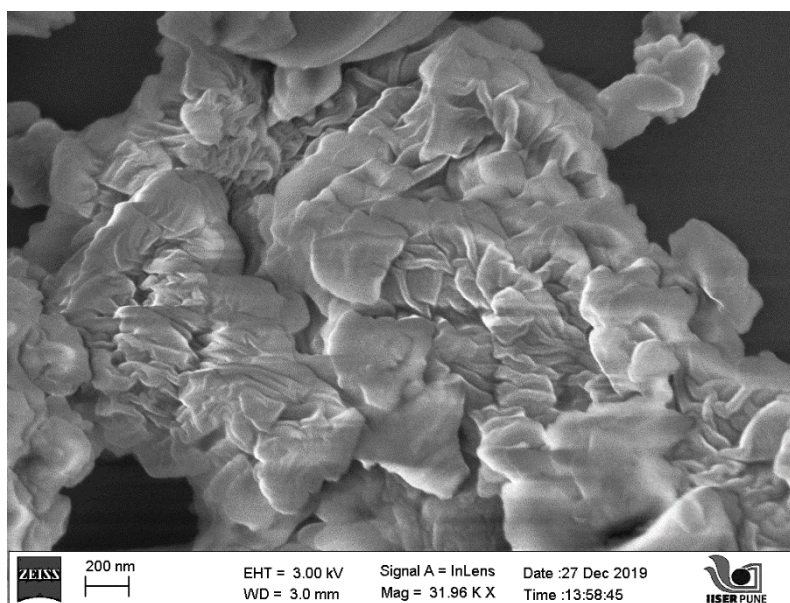


Figure S19. FE-SEM of 3

12. TEM

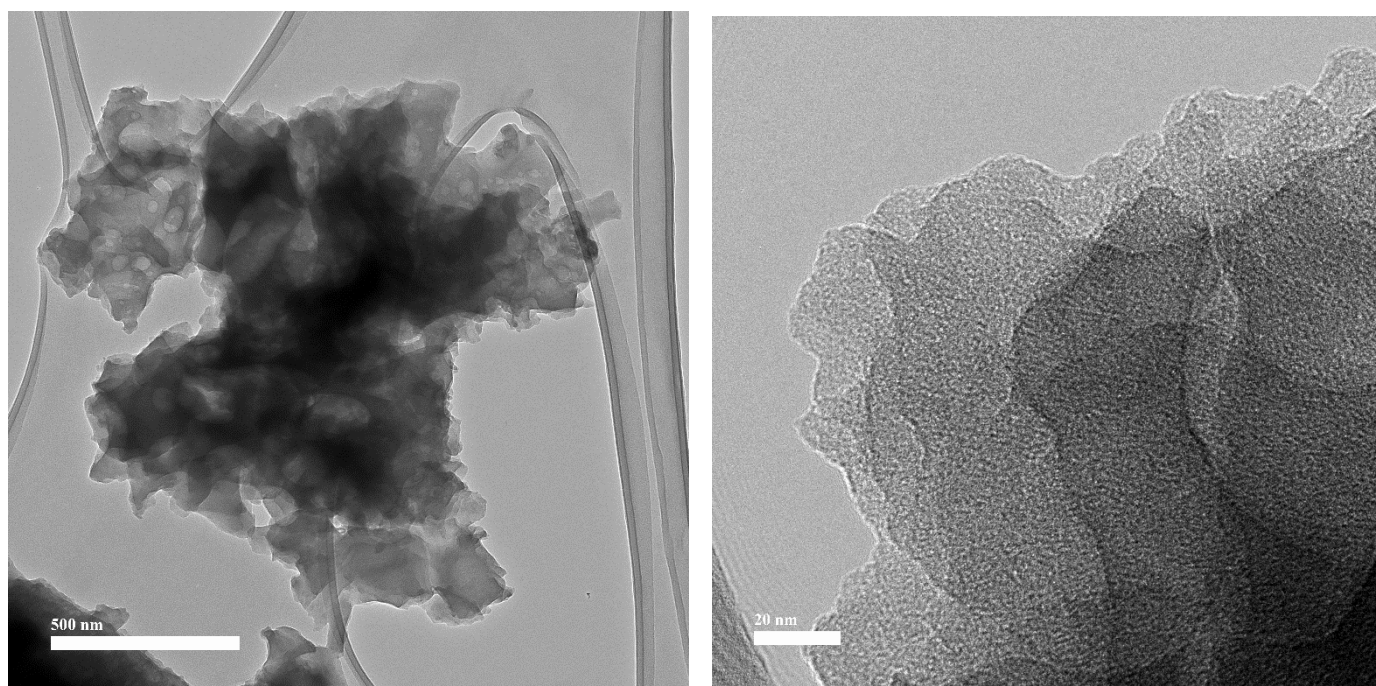


Figure S20. TEM of **3** taken on lacey carbon grid

13. Electrochemical Performance

Table S3. Selective reported examples of *N,O*-containing Carbon Materials

	Material Type	O %	N %	Initial Discharge Capacity	1 st Reversible Capacity	Initial Coulombic Efficiency	Stability	Capacity at Higher current Density
1 ^a	<i>N</i> -doped graphene film	present	09 at%	0.25 mA h/cm ² (at 5 μA/cm ²)	0.08 mA h/cm ² (at 5 μA/cm ²)	32 %	After 50 cycles 0.05 mA h/cm ² (5 μA /cm ²)	0.03 mAh/cm ² (at 100 μA/cm ²)
2 ^b	<i>N</i> -doped Carbon Nano Sheets	10.4 at%	6.4 at%	1100 mA h/g (at 0.1 A/g)	607 mA h/g (at 0.1 A/g)	54%	After 600 cycles 245 mA h/g (500 mA/g)	204 mA h/g (at 1 A/g)
3 ^c	<i>N</i> -doped graphene like Carbon Nano sheets	4.13 %	2.67 %	1052 mA h/g (at 1C)	480 mA h/g (at 1C)	48 %	After 100 cycles 480 mA h/g (1C)	440 mA h/g (at 5C)
4 ^d	<i>N</i> -Doped Carbon Nano particles	7.4 at%	2.6 at%	1190 mA h/g (at 0.1C)	596 mA h/g (at 0.1C)	50 %	After 100 cycles 450 mA h/g (0.1C)	300 mA h/g (at 1C)
5 ^e	<i>N</i> -rich porous carbon sphere	present	5.4 wt%	1100 mA h/g (at 0.5 A/g)	666 mA h/g (at 0.5 A/g)	60 %	After 100 cycles 540 mA h/g (0.5 A/g)	215 mA h/g (at 3 A/g)
6 ^f	<i>N</i> -rich Hybrid Carbon Nano material	6.4 wt%	9.3 wt%	1106 mA h/g (at 100 mA/g)	934 mA h/g (at 100 mA /g)	84 %	After 500 cycles 445 mA h/g (500 mA/g)	215 mA h/g (at 5 A/g)
7 ^g	<i>N</i> -doped hollow carbon sphere	present	12 at %	1012 mA h/g (at 0.1 A/g)	777 mA h/g (at 0.1 A/g)	76 %	After 400 cycles 1064 mA h/g (0.1 A/g)	360 mA h/g (at 10 A/g)
8 ^h	<i>N</i> -doped carbon capsule	present	13 at %	1349 mA h/g (at 50 mA/g)	1217 mA h/g (at 50 mA/g)	90 %	After 50 cycles 1046 mA h/g (50 mA/g)	285 mA h/g (at 20 A/g)

	Material Type	O %	N %	Initial Discharge Capacity	1st Reversible Capacity	Initial Coulombic Efficiency	Stability	Capacity at Higher current Density
9^j	<i>N</i> -doped graphene	present	1.68 at %	1420 mA h/g (at 100 mA/g)	950 mA h/g (at 100 mA/g)	67 %	After 150 cycles 500 mA h/g (200 mA/g)	150 mA h/g (at 5 A/g)
10^j	<i>N</i> -rich mesoporous carbon	present	present	1900 mA h/g (at 0.1 mA/cm ²)	1029 mA h/g (at 0.1 mA/cm ²)	54 %	After 100 cycles 900 mA h/g (0.1 mA/cm ²)	400 mA h/g (at 0.8 mA/cm ²)
11^k	<i>N</i> -rich porous carbon	6.9 at%	5.5 at %	2166 mA h/g (at 100 mA/g)	1290 mA h/g (at 0.1 A/g)	59 %	After 100 cycles 1181 mA h/g (0.1 A/g)	470 mA h/g (at 2 A/g)
12^l	Carbon nanofibers	present	present	847 mA h/g (at 0.5 A/g)	469 mA h/g (at 0.5A/g)	54%	After 100 cycles 450 mA h/g (0.5 A/g)	200 mA h/g (at 8 A/g)
13^m	Multi-functionalized Herringbone Carbon nanofiber	15.3 at%	10.2 at%	1100 mA h/g (at 0.1 A/g)	763 mA h/g (at 0.1 A/g)	69%	After 360 cycles 500 mA h/g (1 A/g)	402 mA h/g (at 3 A/g)
14ⁿ	<i>N</i> -rich porous carbon Nano spheres	present	21.5 wt%	2600 mA h/g (at 100 mA/g)	1378 mA h/g (at 100 mA/g)	53%	After 100 cycles 1070 mA h/g (500 mA/g)	530 mA h/g (at 5 A/g)
15^o	Porous <i>N</i> -doped Carbon Nanoribbons	present	8.4 at%	1189 mA h/g (at 100 mA/g)	792 mA h/g (at 100 mA/g)	67%	After 200 cycles 628 mA h/g (200 mA/g)	320 mA h/g (at 1 A/g)
16^p	<i>N</i> -self-doped graphene	present	2.1 at%	1177 mA h/g (at 50 mA/g)	850 mA h/g (at 50 mA/g)	72%	After 95 cycles 682 mA h/g (50 mA/g)	439 mA h/g (at 2 A/g)
17^q	<i>N</i> -doped Amorphous Carbon	present	11.77 at%	1722 mA h/g (at 0.2 C)	699 mA h/g (at 0.2 C)	41%	After 600 cycles 466 mA h/g (0.5 C)	130 mA h/g (at 20 C)
18^r	<i>N, O</i> -containing Carbon Material	11.94 wt%	10.01 wt%	2072 mA h/g (at 100 mA/g)	1071 mA h/g (at 0.1 A/g)	52 %	After 150 cycles 840 mA h/g (100 mA/g)	300 mA h/g (at 4 A/g)

a) A. L. M. Reddy, A. Srivastava, S. R. Gowda, H. Gullapalli, M. Dubey and P. M. Ajayan, *ACS Nano*, 2010, **4**, 6337.

b) A. K. Radhakrishnan, S. Nair, D. Santhanagopalan, *J. Mater. Res.* DOI: 10.1557/jmr.2019.330.

- c) D. Damodar, S. Krishna Kumar, S. K. Martha b and A. S. Deshpande, *Dalton Trans.* 2018, **47**, 12218.
d) D. Bhattacharjya, H. -Y. Park, M. -S. Kim, H. -S. Choi, S. N. Inamdar, and J. -S. Yu, *Langmuir* 2014, **30**, 318.
e) D. Li, L. -X. Ding, H. Chen, S. Wang, Z. Li, M. Zhu and H. Wang, *J. Mater. Chem. A*, 2014, **2**, 16617.
f) B. P. Vinayan, N. I. Schwarzburger and M. Fichtner, *J. Mater. Chem. A*, 2015, **3**, 6810.
g) Y. Tang, X. Wang, J. Chen, X. Wang, D. Wang and Z. Mao, *Carbon*, 2020, **168**, 458.
h) C. Hu, Y. Xiao, Y. Zhao, N. Chen, Z. Zhang, M. Cao, and L. Qu, *Nanoscale*, 2013, **5**, 2726.
i) Z. Xing, Z. Ju, Y. Zhao, J. Wan, Y. Zhu, Y. Qiang, and Y. Qian, *Sci. Rep.* 2016, **6**, 26146.
j) Y. Mao, H. Duan, B. Xu, L. Zhang, Y. Hu, C. Zhao, Z. Wang, L. Chen and Y. Yang, *Energy Environ. Sci.* 2012, **5**, 7950.
k) J. Ou, Y. Zhang, L. Chen, Q. Zhao, Y. Meng, Y. Guo, and D. Xiao, *J. Mater. Chem. A*, 2015, **3**, 6534.
l) Z. Shen ,Y. Hu ,Y. Chen ,R. Chen ,X. He ,L. Geng ,X. Zhang, and K. Wu, *Small* 2016, **12**, 5269.
m) M. -H. Kim, M. -Y. Cho, K. -B. Kim, H. G. Jeong, J. T. Han and K. C. Roh, *Phys.Chem.Chem.Phys.* 2017, **19**, 18612.
n) Z. Xie, Z. He, X. Feng, W. Xu, X. Cui, J. Zhang, C. Yan, M. A Carreon, Z. Liu, Y. Wang, *ACS Appl. Mater. Interfaces*, 2016, **8**, 10324.
o) Q. -S. Yang, Z. -Y. Sui, Y. -W. Liu, and B. -H. Han, *Ind. Eng. Chem. Res.*, 2016, **55**, 6384.
p) C. He, R. Wang, H. Fu, and P. K. Shen, *J. Mater. Chem. A*, 2013, **1**, 14586.
q) W. Guo, X. Li, J. Xu, H. K. Liu, J. Ma and S. X. Dou, *Electrochim. Acta*, 2016, **188**, 414.
r) This work

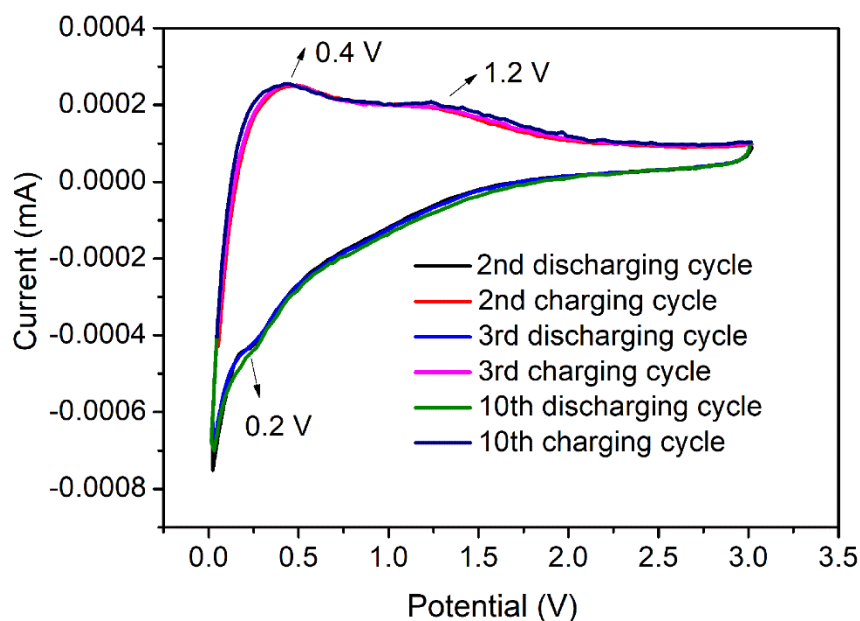


Figure S21. Cyclic Voltammogram (scan rate = 0.2 mV/sec) of the electrode containing **3** in the half-cell w.r.t. Li/Li⁺

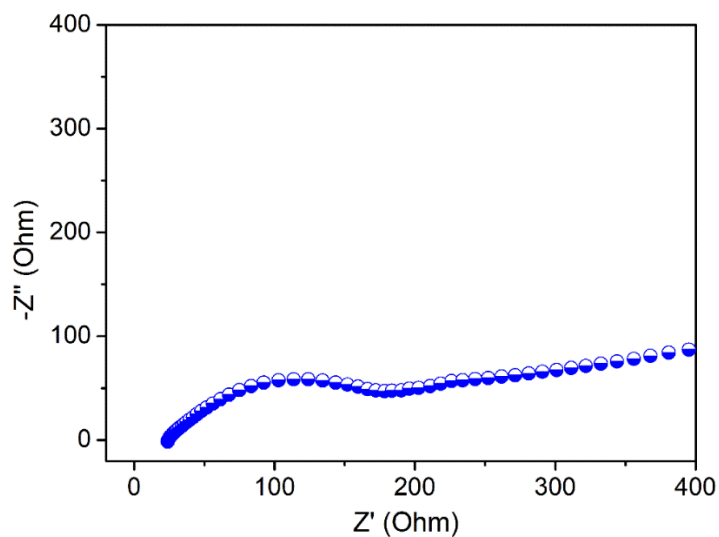


Figure S22. Nyquist plot (electrochemical impedance spectroscopy data) of the electrode containing **3** in the half cell.

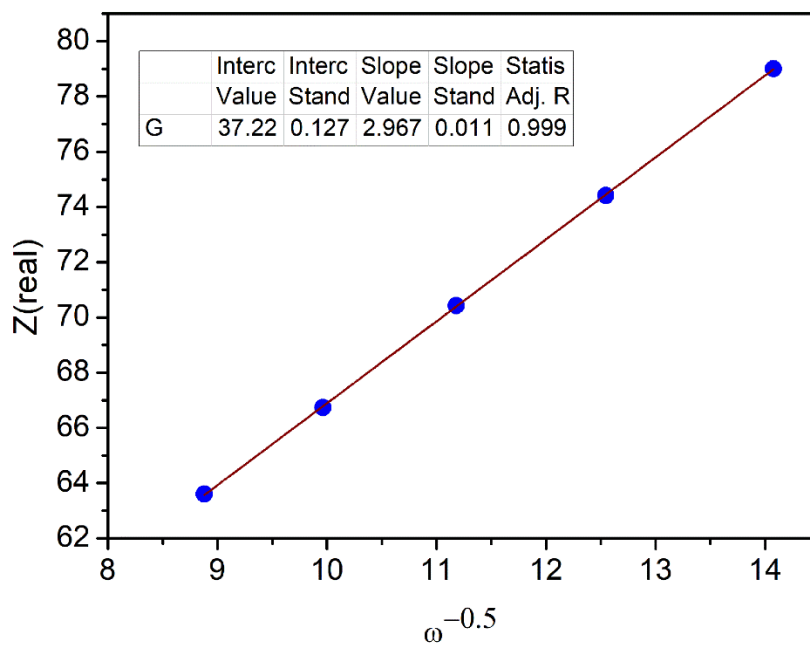


Figure S23. Plot of $Z(\text{real})$ vs. $\omega^{-0.5}$ to determine Warburg coefficient from electrochemical impedance spectroscopy data of **3** in the half cell

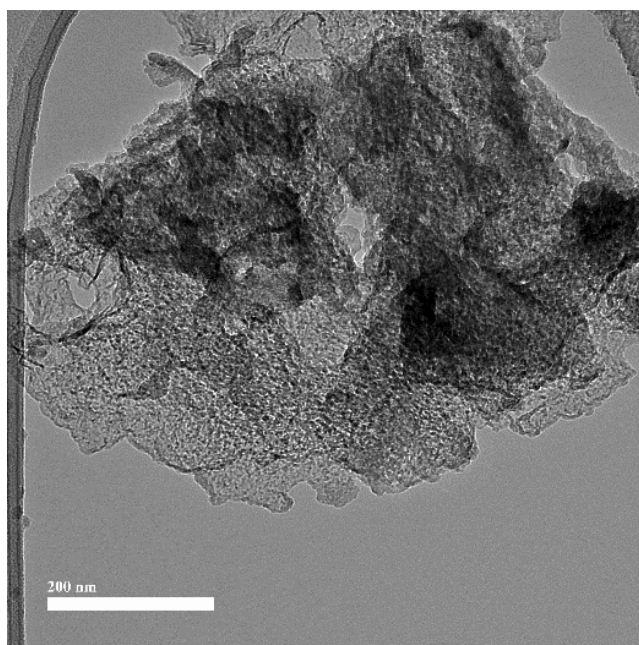


Figure S24. HRTEM image after 394 charge-discharge cycles of **3** as anode material on lacey carbon grid (200 nm scale bar) showing the sheet-like morphology remains intact although highly amorphous in nature.

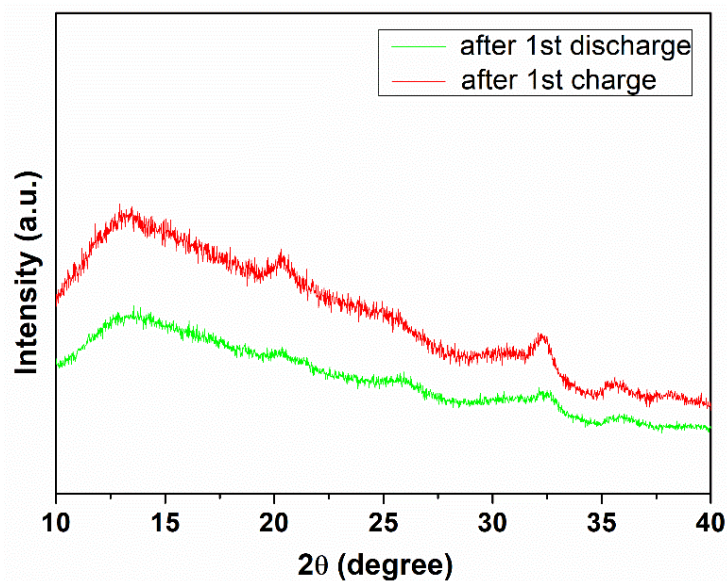


Figure S25. Post-cycling grazing incidence XRD of **3** showing intercalation/de-intercalation of Li ions ($2\theta = 13\text{-}20^\circ$) into the carbon with no major structural changes.

References

- [S1] T. Saito, H. Nishiyama, H. Tanahashi, K. Kawakita, H. Tsurugi, K. Mashima, *J. Am. Chem. Soc.* 2014, **136**, 5161-5170.
[S2] A. Doughty, J. C. Mackie and J. M. Palmer, *Twenty Fifth Symposium (International) on Combustion/The Combustion Institute*, 1994, 893-900.
[S3] Gaussian 09, Revision E.01, M. J. Frisch, G. W. Trucks, H. B. Schlegel, G. E. Scuseria, M. A. Robb, J. R. Cheeseman, G. Scalmani, V. Barone, B. Mennucci, G. A. Petersson, H. Nakatsuji, M. Caricato, X. Li, H. P. Hratchian, A. F. Izmaylov, J. Bloino, G. Zheng, J. L. Sonnenberg, M. Hada, M. Ehara, K. Toyota, R. Fukuda, J. Hasegawa, M. Ishida, T. Nakajima, Y.

Honda, O. Kitao, H. Nakai, T. Vreven, J. A. Montgomery, Jr., J. E. Peralta, F. Ogliaro, M. Bearpark, J. J. Heyd, E. Brothers, K. N. Kudin, V. N. Staroverov, R. Kobayashi, J. Normand, K. Raghavachari, A. Rendell, J. C. Burant, S. S. Iyengar, J. Tomasi, M. Cossi, N. Rega, J. M. Millam, M. Klene, J. E. Knox, J. B. Cross, V. Bakken, C. Adamo, J. Jaramillo, R. Gomperts, R. E. Stratmann, O. Yazyev, A. J. Austin, R. Cammi, C. Pomelli, J. W. Ochterski, R. L. Martin, K. Morokuma, V. G. Zakrzewski, G. A. Voth, P. Salvador, J. J. Dannenberg, S. Dapprich, A. D. Daniels, Ö. Farkas, J. B. Foresman, J. V. Ortiz, J. Cioslowski, and D. J. Fox, Gaussian, Inc., Wallingford CT, 2009.

[S4] X-ray data matches well with the earlier literature report: A. W. M. Braam, J. C. Eikelenboom, G. Van Dijk, A. Vos, *Acta Cryst.* 1981, **B37**, 259-261.